THE AMERICAN SOCIETY OF MECHANICAL ENGINEERS
345 E. 47th St., New York, N.Y. 10017

96-GT-376

INLET DISTORTION GENERATED FORCED RESPONSE OF A LOW ASPECT RATIO TRANSONIC FAN

Steven R. Manwaring
GE Aircraft Engines
Cincinnati, Ohio U.S.A.

Douglas C. Rabe
Wright Laboratory
Wright–Patterson AFB, OH U.S.A.

Christopher B. Lorence and **Aspi R. Wadia**
GE Aircraft Engines
Cincinnati, Ohio U.S.A.

ABSTRACT

This paper describes a portion of an experimental and computational program (ADLARF) which incorporates, for the first time, measurements of all aspects of the forced response of an airfoil row, i.e., the flow defect, the unsteady pressure loadings and the vibratory response. The purpose of this portion was to extend the knowledge of the unsteady aerodynamics associated with a low aspect ratio transonic fan where the flow defects were generated by inlet distortions. Measurements of screen distortion patterns were obtained with total pressure rakes and casing static pressures. The unsteady pressure loadings on the blade were determined from high response pressure transducers. The resulting blade vibrations were measured with strain gages. The steady flow was analyzed using a 3D Navier–Stokes solver while the unsteady flow was determined with a quasi–3D linearized Euler solver.

Experimental results showed that the distortions had strong vortical, moderate entropic and weak acoustic parts. The 3D Navier–Stokes analyses showed that the steady flow is predominantly two–dimensional, with radially outward flow existing only in the blade surface boundary layers downstream of shocks and in the aft part of the suction surface. At near resonance conditions, the strain gage data showed blade–to–blade motion variations and thus, linearized unsteady Euler solutions showed poorer agreement with the unsteady loading data than comparisons at off–resonance speeds. Data analysis showed that entropic waves generated unsteady loadings comparable to vortical waves in the blade regions where shocks existed.

NOMENCLATURE

b	Semi–chord at 85% span = C/2
C	Speed of sound, Chord at 85% span
C_m	Chord at midspan
$C'_{\Delta p}$	Unsteady pressure difference coefficient = $\Delta p_s'/(0.5\rho W^2)/(w'/W)$
F_G	Modal force per chordwise section
G	Damping of blade
H_{SA}	Blade height at stacking axis
LAR	Low aspect ratio
LOL	Low operating line
k	Reduced frequency = ωb/W
K	Stiffness of blade
M	Inertia of blade
Ma	Steady absolute Mach number
NOL	Nominal (Design) Operating Line
p_s'	First harmonic of unsteady static pressure
s	Surface distance around blade surface
S	Span
TE	Trailing Edge
T	Blade tangential spacing at midspan
T_m	Maximum thickness
U	Blade Speed
V	Steady Absolute Velocity
v_x'	First harmonic of unsteady axial velocity
v_y'	First harmonic of unsteady tangential velocity
W	Steady Relative Velocity
X	Blade motion
δ	Blade motion deflection
ε	Blade vibratory strain
λ	Characteristic of first harmonic of unsteady flow
ρ'	First harmonic of unsteady density
ω	Frequency of flow defect excitation, rad/s
ω_n	Natural frequency of blade mode, rad/s
ζ	Blade total system damping

Subscripts

FE	Finite element solution
G	Location of strain gage
MS	Measurement
n	Normal to blade surface

Presented at the International Gas Turbine and Aeroengine Congress & Exhibition
Birmingham, UK — June 10-13, 1996
This paper has been accepted for publication in the Transactions of the ASME
Discussion of it will be accepted at ASME Headquarters until September 30, 1996

INTRODUCTION

The development process for modern turbomachinery blading can be greatly improved with accurate predictions of blade unsteady aerodynamic loadings which are in turn used to predict blade resonant amplitudes. In the design process, excitation frequencies and mode frequencies are adjusted to ensure that crossings do not occur in the higher speed ranges where vibrations may cause fatigue failures. However, with modern low aspect ratio (LAR) blading, modal compression occurs (mode frequencies are more closely packed) and thus, the designer is forced to accept crossings at higher speeds where significant vibrations may occur. Therefore, accurate predictions of blade unsteady loads and subsequent vibrational response are necessary to determine if resonance crossings can be tolerated.

In recent years a number of computational methods for unsteady flows have been developed. Several authors have calculated unsteady periodic flows by time–accurately marching the Euler (Whitfield et al, 1987; Giles, 1988) or Navier–Stokes (Huff, 1987; Rai, 1989) equations. Unfortunately, because of the significant computational expense associated with these analyses, they are best suited for occasional unsteady aerodynamic analysis, not for routine design.

To reduce this computational expense, linearized unsteady solution methods have been developed. In these schemes, the flow is assumed to be composed of a nonlinear steady flow plus a small harmonic unsteady flow. In general, these approaches require one to two orders of magnitude less computational time than their time–marching counterparts. Verdon and Caspar (1984) and Whitehead (1990) have developed linearized analyses for transonic flows using the potential equation. Potential methods, however, do not model strong shocks such as those found in LAR fans. A more suitable method, developed by Hall and Crawley (1989), is to use the linearized Euler equations. Recently, a number of linearized Euler analyses have been developed for 2D and quasi–3D flows (some examples are Hall and Clark, 1993; Holmes and Chuang, 1993) as well as for fully 3D flows (Hall and Lorence, 1993).

To understand the physical mechanisms and to determine the abilities and accuracies of these computational predictions, high quality data are needed where the measurements are taken on a modern design while operating at realistic flow conditions. A complete data set defining the aeroelastic excitation and response of a fan must include measurements of the flow defect, the blade unsteady loading and the resulting vibrational response.

However, prior experimental programs have incorporated only half of the full forced response problem, i.e., either gust response or oscillating airfoil response, and have been limited to 2D, unsteady flow models. Fleeter and his colleagues (Fleeter, et. al., 1978 and 1980; Capece and Fleeter, 1987; Manwaring and Fleeter, 1990 and 1993; and Henderson and Fleeter, 1993) have measured the midspan unsteady pressures on low speed compressor blading where gusts were generated from distortions, wakes and potential fields. In these experiments the airfoils are rigid and do not respond to the gusts. Gallus, Lambertz and Wallman (1980) performed rigid airfoil, gust response experiments on the midspan of an axial flow compressor. Manwaring and Wisler (1993) obtained gust response measurements for low speed compressor and turbine blading. For blade motion experiments, Boles and Fransson (1986) measured the midspan sections of compressor and turbine airfoils in an annular cascade where the airfoils were actuated. Buffum and Fleeter (1990) have obtained unsteady pressure measurements on the blade surfaces of a linear cascade of compressor blading also using an actuation system to provide blade motion.

Thus, there is need for additional data and analysis in a 3D, transonic unsteady flow environment. Therefore, a series of experiments were performed, where inlet distortions were generated and measurements of the unsteady pressure loadings and the resulting vibrations were made. The objective of this work is to further understand the physical mechanisms of the aeroelastic excitation and unsteady aerodynamic response in a 3D transonic fan rotor. The unsteadiness is generated by both upstream disturbances and blade motions. Evaluation of current state–of–the –art design capabilities will be made.

Table 1. Rotor 1 Design Parameters

Number of Blades	16
Aspect Ratio, C_m/H_{SA}	1.0
Solidity, C_m/T	1.8
Tm/C at tip	0.028
Midspan Chord, cm	19.0
85% Span Chord, cm	20.4
Material	Ti 6–4
Tip Radius, cm	35.2
Tip Speed, m/s	490.4
Design Flow, Kg/s	71.95
Design Speed, RPM	13,288

The following analyses were performed to help meet this objective. 3D Navier–Stokes analyses were used to understand the steady flow environment more fully. Quasi–3D, linearized unsteady Euler predictions were obtained to assess their capabilities for LAR fans. This unsteady flow analysis was performed by specifying the gust and motion boundary conditions from measurements. Future work will be to perform the full forced response prediction wherein the unsteady stress is predicted and then compared to the measurements from the strain–gages.

EXPERIMENTAL PROGRAM

Facility and Test Article

The measurements were obtained in the Compressor Research Facility (CRF) at Wright–Patterson Air Force Base. The CRF is an open cycle tunnel with a 6.10 meter (20ft) diameter test section. An electric motor provides power to the fan, which for this test has a 0.7m diameter rotor setting centered in the tunnel. Atmospheric filtered air is drawn through five inlet valves which control inlet pressure. For this program near atmospheric inlet conditions were maintained.

The machine tested was a 2–stage fan with the first stage being a low aspect ratio (LAR) design. Table 1 shows the geometric and aerodynamic design parameters of this instrumented first stage rotor. The compressor was designed for high axial flow, which gives transonic conditions in the outer half of the first stage rotor. Data were acquired at two conditions, low operating line (LOL) and design or nominal operating line (NOL). The LOL was obtained at the full open throttle condition and the NOL was determined by the peak efficiency point of the speed line. Due to the risk of damaging sensor during a possible stall event, data were not acquired at a near stall condition. Data and analysis at the NOL is presented in this paper.

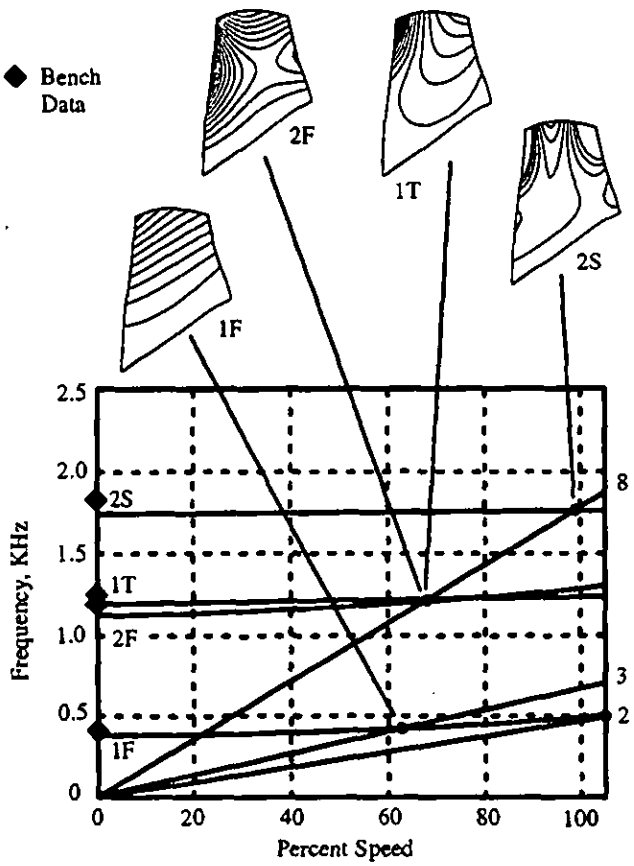

Figure 1. Predicted Campbell diagram and measurements at zero speed

Inlet screens of two, three and eight periods per revolution were used to generate distorted flow. The screens were mounted on a circumferential rotator to allow for different angular positions to be obtained while the machine is in operation. The predicted Campbell diagram in Figure 1 shows that the follnwing four resonance crossings occur during the fan operation: 3/rev –first flex (1F) at 62% speed, 8/Rev – second flex/first torsion (2F/1T) at 68% speed, 8/rev –two stripe (2S) at 98% speed, and 2/rev – 1F near 105% speed. During testing the anticipated 2/rev –1F crossing at 105% was not obtainable. The predicted mode shapes for each of the crossings are also shown in Figure 1.

Instrumentation

Steady Aerodynamic Performance. The overall steady performance was determined at several speeds from measurements of the overall flow and total temperature and pressure. The flow was obtained from a calibrated venturi at the exit of the test section. To determine the radial profiles of temperatures and pressures, rakes were located at the inlet, inlet to stator 1 and 2 and stator 2 exit.

Flow Distortion. The measurements of the circumferential variation in total pressure due to the screens were obtained with eight five–element rakes located 37 cm (14.6 in.) upstream of the leading edge at the blade root as shown in Figure 2. For each rake, a static pressure at the casing was measured using a tap located 10° from the rake. For the 3/rev distortion, measurements were taken at four screen rotations to give 32 points around the circumference or 10.67 points per period of the distortion. For the 8/rev distortion, ten screen rotations gave 10 points per period. For both the rake and casing static pressures, measurements were accurate to within ±0.002 atm, which is ±4.0% of the lowest dynamic pressure at the inlet encountered during the three crossings of interest.

Blade Unsteady Loading. The unsteady pressure difference across the blade was measured with Kulite model XCQ–093 dynamic pressure transducers with a 50 psid range. The transducers were located at 85% span on two adjacent blades, numbers 1 and 16 as shown in Figure 3. Both of the blades had seven transducers located in identical chordwise positions. The accuracy of the transducers was ± 0.031 atm., which is approximately 25% of the maximum measured periodic unsteadiness. During data acquisition the upstream rakes used for measuring distortions were removed to ensure blade unsteady loadings were only due to screen generated distortions.

Several transducer signals failed during testing, presumably due to the centrifugal loads encountered. At 62% speed 8 of the original 14 transducers were operational. At 68% speed, on a subsequent run, three of the sporadically failing transducers returned to give 11 measurements. At the high speeds only 5 of the original 14 had survived.

As a demonstration of the difficulty in measuring unsteady pressures on high–speed blading, the original instrumentation of the rotor did not survive the first minutes of operation and the blade was re–instrumented with pressure transducers. The first set of instrumentation failed due to the epoxy used in mounting the sensor diaphragms transmitting excessive blade strain into the sensor and causing failures. The second set of instrumentation used RTV to mount the diaphragms. The intent of this more flexible mounting was to prevent high strain from damaging the sensor. The failures for this testing were mostly attributed to lead wire breaks. For future testing, it is suspected that sputtering the leads directly to the blade surfaces will help retain on–blade measurements.

The transducers were embedded flush to one surface of the blade and pneumatically connected to the other surface with a vent hole in order to sense the differential unsteady pressures across the blade. The maximum vent hole length was 4.72 mm (0.120 in). The natural frequency of the installation system is 20 kHz. The highest excitation frequency encountered is 1.9 kHz for the 8/rev distortion at 98% speed which is well within the flat response range of the transducer/installation system. Therefore, dynamic calibration of the measurement system was deemed unnecessary. The transducer sensitivities were determined from calibrations performed by the transducer manufacturer. Rabe, Bolcs and Russler (1995) show in more detail the installation of the transducers and typical unsteady pressure measurements encountered during testing in this program.

Vibratory Response. Vibratory stresses were obtained by dynamic strain gages applied to the blade surfaces. Root strain gages were located on the pressure surfaces of the two Kulite instrumented blades and two other blades located roughly 120° around the circumference of the blade row. These gages were located to be sensitive to the 1F, 2F and 1T modes. Trailing edge (TE) gages were located on the two Kulite instrumented blades to accurately measure the 2S chordwise–bending mode. However, during testing these TE gages failed almost immediately. Thus, the root gages have been used to determine amplitudes of the 2S deflections.

Data Reduction

Steady Aerodynamic Performance. To determine the detailed steady performance of the 2–stage LAR fan, radial profiles of the circumferentially–averaged total pressure and temperature were used to define the

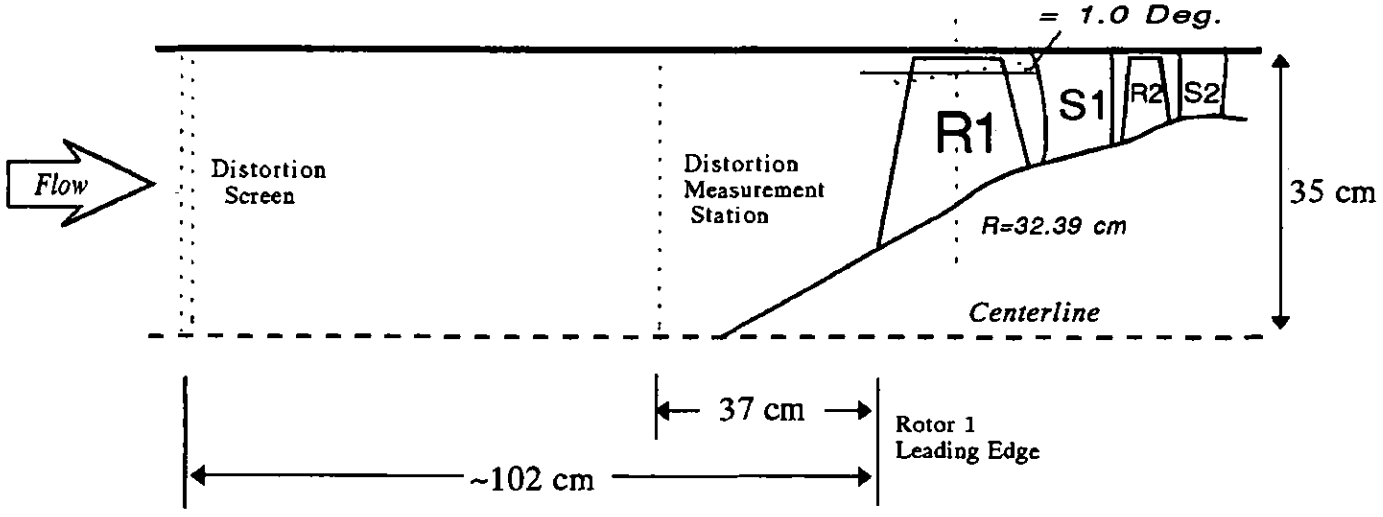

Figure 2. Test fan and generation of distortion

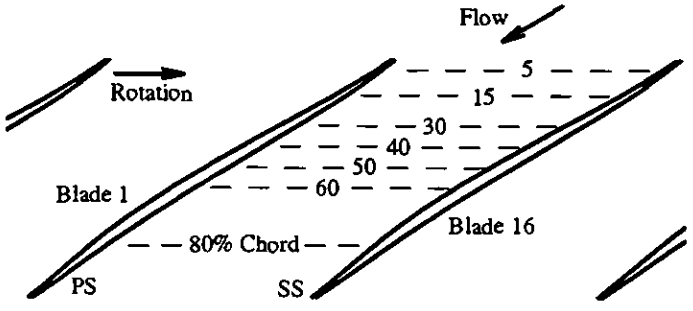

Figure 3. Locations of blade–mounted pressure transducers at 85% span

intra–blade row conditions. These profiles and the speed and mass flow set the flow properties for a streamline–curvature, radial–equilibrium analysis. This throughflow analysis was then used to set the initial and boundary conditions of the computational analyses.

Flow Distortion. The "per rev" content of the excitation of the first stage rotor was calculated from the Fourier decomposition of the circumferential distributions of measured total and casing static pressures. The variation in static pressure from its average value at the casing is normalized by the local value of the dynamic pressure obtained from the throughflow analysis. This normalized static pressure variation is assumed to remain constant across the span. Circumferential variation in total pressure at any span location is obtained by interpolating or extrapolating each harmonic and then reconstructing the distribution. The circumferential variation in velocities and densities at desired span locations can be calculated by using these pressure variations and the total temperature measurements. Fourier decomposition of these circumferential surveys at different spanwise locations give radial profiles of the first harmonic disturbance in terms nf primitive variable perturbations, ρ', v_x', v_y' and p_s'. The screens were designed to give pure tone disturbances, which were verified by second harmonic magnitudes being less than 5% of the first harmonics for both screens, 3/rev and 8/rev.

The primitive variable definition of the unsteadiness to the blade can be used to specify proper incoming boundary conditions for unsteady analyses. However, these definitions do not give a clear understanding of the physical mechanisms generating the unsteadiness. Giles (1988) and others have used an eigen–analysis of the 2D Euler equations to determine the relationship between primitive variable perturbations and natural modes of the unsteady flowfield. There are four natural modes (characteristics) of the system: an entropy wave (λ_1), a vorticity wave (λ_2), one downstream moving pressure wave (λ_3), and one upstream moving pressure wave (λ_4). Because only incoming disturbances at the upstream boundary are of interest in this case, (λ_4) need not be calculated. A modified version of Giles' transformation may he used here, then, to compute the magnitudes and phases of the incoming characteristics. By describing the steady flow in the stationary versus rotating reference frame and setting the steady tangential velocity to zero, purely axial flow at the measurement plane (radial velocity is nearly zero), the following is obtained.

$$\begin{bmatrix} \rho' \\ v_x' \\ p_s' \end{bmatrix} = \begin{bmatrix} \frac{-M_a}{2} & 0 & \frac{U}{2VC^2}\frac{M_a}{\sqrt{M_a^2-1}} \\ 0 & \frac{-U}{2C} & \frac{-U}{4C}\frac{1}{\sqrt{M_a^2-1}} \\ 0 & 0 & \frac{U}{2V}\frac{M_a}{\sqrt{M_a^2-1}} \end{bmatrix} \begin{bmatrix} \lambda_1 \\ \lambda_2 \\ \lambda_3 \end{bmatrix} \quad (1a)$$

$$v_y' = \frac{\sqrt{M_a^2-1}}{2} p_s' \quad (1b)$$

The characteristics can be determined by inverse matrix manipulation. In the above set of equations, the characteristics, λ_i, have been normalized by the dynamic pressure, $0.5\rho V^2$, as well as the static pressure perturbation. The velocity perturbations have been normalized by the steady absolute velocity and the density perturbation by the steady density. The amplitudes and phases of the vortical and entropic waves are assumed to remain constant from the rake measurement axial location to the grid boundary of the computational analysis described below. The acoustic wave amplitude decays exponentially with axial distance.

Blade Unsteady Loads. The procedure used to obtain the unsteady pressure difference acting on the rotor measured by the transducers at 85% span is summarized below. Complete details may be found by refer-

ring to Woehr and Manwaring (1995). The signals were digitized from analog tape at sample rates that would give at least 50 points per period.

An "induced" pressure signal is obtained from two sources: the blade vibration transmitting strain into the transducer diaphragm, and the vibration of the diaphragm. To determine the relationship between transducer signal and vibratory strain for each of the modes that were encountered during testing, the instrumented blade was vibrated in a vacuum chamber. Then by using the measured strain during the tests the "induced" signal was calculated and then subtracted from the measured value of unsteady pressure. In all cases this "induced" signal was small compared to the unsteadiness generated by unsteady aerodynamics from the gusts and blade motions. The largest relative value was for the 1T mode where the mechanically induced signal was 2% of the total signal. The use of flexible RTV for mounting the sensor diaphragm helps keep blade vibratory strain from being transmitted to the transducer sensor.

The unsteady pressure difference is presented as the unsteady pressure on the pressure surface minus the unsteady pressure on the suction surface. The unsteady pressure difference is normalized by the relative dynamic pressure and normalized velocity perturbation as shown below in the definition of the unsteady pressure difference coefficient.

$$C'_{\Delta p} = \frac{\Delta p_s'}{\frac{1}{2}\rho W^2\left(\frac{w'}{W}\right)} \qquad (2)$$

The phases of the blade number 16 signals were adjusted by the interblade phase angle for comparisons with measurements from blade number 1. Since the flow defect is measured in the stationary reference frame, the phase of the pressures cannot be related to the forcing function in an absolute sense. Thus, comparisons between data and analyses can only be of chordwise trends and not absolute phase. For presentation purposes, the pressure data phase levels are adjusted for ease of comparison with the linearized Euler analyses.

Vibratory Response. The strain gage data were stored on analog tape simultaneously with the pressure transducer signals. The strain gage signals were digitized and Fourier analyzed to give amplitude and phase of the measured strain. During speed transients, near real time Fourier amplitudes are obtained at discrete frequencies versus time (speed) which are then plotted in Campbell Diagram format.

COMPUTATIONAL PROGRAM

This section describes the computational modeling of the blade mode shapes and the steady and linearized unsteady aerodynamics of the first stage LAR rotor.

Blade Mode Shapes

Finite element modeling was used to determine the mode shapes for the stage 1 blade. Only the airfoil was included in the model due to the high relative stiffness of the rest of the structure. Twenty brick elements were used in the chordwise and spanwise directions. Four elements were used through the thickness. Good agreement of frequencies and mode shapes was found between bench tests and analytical results for zero speed as can be seen in Figure 1. Finite element analyses, including large deflection, stress stiffening, and spin softening options were used for the predictions. The mode shapes resulting from this analysis were used as surface boundary conditions for the blade unsteady loading calculations described below. In addition, the stress predictions were used to correlate the measured vibratory response from the strain gages to the modal amplitude.

Steady Aerodynamics

The prediction of the 3D steady flow was obtained from a 3D Navier Stokes solver, Turner and Jennions (1992). The grid used for these viscous calculations consisted of 260,000 nodes with 117 cells in the streamwise direction, 48 in the blade–to–blade direction, and 44 in the radial direction, 4 being in the tip gap region. K–ε turbulence modeling was used and wall functions were used for the boundary layer flow very close to the endwall and blade surfaces. Boundary and initial conditions were obtained from the streamline–curvature/data–match analysis described earlier. The blade untwist going from design speed to the part speed conditions was assumed to have negligible effect on the steady and unsteady flow solutions so all computational analyses used the design speed geometry definitions.

Unsteady Aerodynamics

The unsteady aerodynamics is predicted with a quasi–3D linearized Euler solver where the steady flow is calculated with the full non–linear Euler equations. The steady boundary conditions are obtained from the streamline–curvature/data–match analyses. The definition of the unsteady boundary conditions was described in the previous sections. The steady flow of the quasi–3D analysis was "tuned" to match the steady flow predicted by the 3D Navier–Stokes solver described above. "Tuning" was achieved by adjusting the streamtube thickness distribution through the blade until the surface ideal Mach numbers nearly matched those of the viscous solution.

The linearized Euler analysis used in this paper (Holmes and Chuang, 1993) uses an unstructured, adaptive finite–volume scheme. The Euler equations are solved in conservation–law form with shock capturing used to model the shock impulse. Unlike subsonic flows, where solutions are weakly dependent on grid resolution, transonic flows are strongly dependent on the number of grid points used as well as the artificial viscosity in the scheme. In principle, shocks may be increasingly refined until they have negligible width. While this may be useful from a code validation standpoint, such highly refined shocks are not representative of actual viscous flows. As a result, the quasi–3D grids used here were only moderately refined so as to simulate the 3D viscous flow environment while maintaining sufficient resolution to predict the unsteady flowfield accurately. Numerical experiments have shown that additional grid refinement only produces more refined shocks, without significantly affecting the rest of the flowfield. In addition, the wavelengths of the unsteady disturbances have been computed analytically to ensure that the grids used appropriately resolve these waves. This approach is not without precedent. Lindquist and Giles (1994) and Hall et al (1994) have shown that unsteady shock loads can be modeled accurately using linearized Euler analyses if the scheme is conservative and the shocks are sufficiently smeared.

The blade motion surface boundary conditions for the unsteady aerodynamic analyses are obtained from the finite element mode shape predictions and the root strain gage measurements. The amplitude of the deflections at any point on the blade is related to the strain at the root gage by the following equation.

$$\delta_i = \delta_{i,FE}\left(\frac{\epsilon_{G,MS}}{\epsilon_{G,FE}}\right) \qquad (3)$$

where FE subscripts denote finite element predicted strains and deflections and MS subscript denotes measured strain.

Before the gust and blade motion unsteady solutions can be superimposed, the unsteady loadings must be properly phase related. The relationship between the gust and the blade motion is described with the following

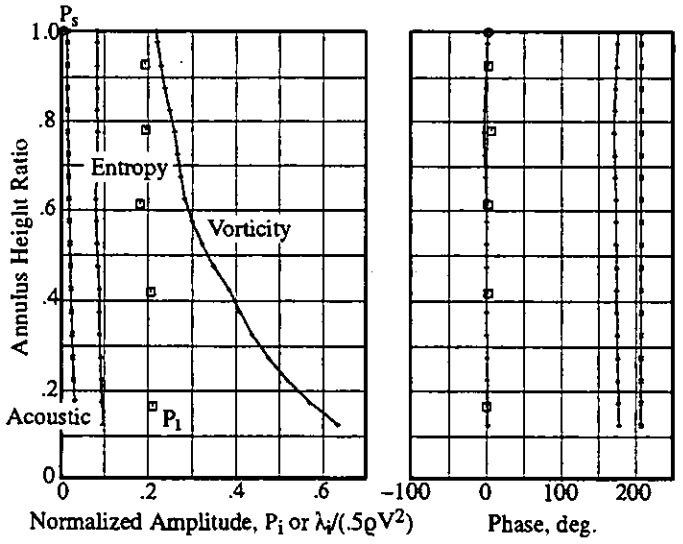

Figure 4. First harmonic of pressures and flow defect characteristics from 3/rev distorted flow at 62% speed

single–degree–of–freedom (SDOF) equation

$$M\ddot{X} + G\dot{X} + X = F_G \tag{4}$$

where X is the blade motion and F_G is the modal force of the gust. The modal force at the 85% span section is obtained by integrating the unsteady pressure times the modal deflections around the surface of the blade as the following equation shows

$$F_G = \oint p_s'(s)\, \delta_n(s)\, ds \tag{5}$$

where p_s' and F_G are complex and δ_n is real and s is surface distance around the blade. Solving the differential equation shown above for SDOF motion, Equation 4, the following relationship is obtained

$$\frac{X}{F_G} = \frac{1}{\left[\left(\frac{i\omega}{\omega_n}\right)^2 + 2\zeta\left(\frac{i\omega}{\omega_n}\right) + 1\right]} \tag{6}$$

where ζ is the total system damping and is obtained by applying the half–power law to the resonance amplitude versus frequency (RPM) distribution measured with the root strain gages. For typical solutions of Equation 6, the gust is assumed to be real (zero phase) and the phase of the motion is determined from Equation 6. However, for these analyses, the blade motion, X is real (phase of zero) and Equation 6 will quantify the amount that the gust leads the motion. The phase levels of the predicted gust generated unsteady pressures, p_s', were re–referenced to ensure that the gust force, F_G leads the motion by the correct amount.

RESULTS

This section presents the results of the data and analysis of the steady and unsteady loading during the three crossings encountered during compressor operation with the two distortion screens. The details are presented starting with the lowest speed crossing and proceeding to the highest speed crossing, all at the design (nominal) operating line. For each crossing, analysis of the flow distortions is given followed by presentation of the strain

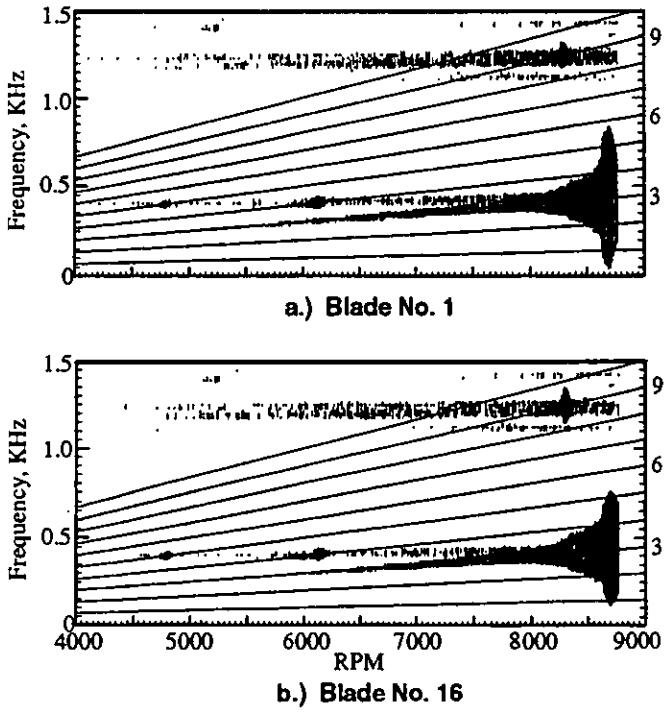

Figure 5. Measured Campbell diagram for 3/rev distortion excitation near 62% speed

gage measurements and mode shapes. Then the predictions of the steady flow through the rotor are discussed. Finally, unsteady loading data and analysis results are shown for off–resonance and near resonance.

3/Rev–1F crossing at 62% Speed

The Fourier decomposition of the circumferential distributions of total pressure and casing static pressure due to the distorted flow from the 3/rev screen is shown in Figure 4. The spanwise profile of normalized amplitude and phase of the first harmonic of the total pressure is nearly uniform and approximately 20% of the dynamic pressure. The casing static pressure first harmonic is less than 1% of the dynamic pressure. The spanwise profiles of the entropy, vorticity and acoustic characteristics calculated from the pressure and total temperature data are also shown in Figure 4. The vortical wave is the strongest of the three, varying from 20% nf the dynamic pressure at the casing to over 70% at the hub. The entropy wave is weaker, being only 8 to 9% of dynamic pressure. The acoustic wave is small, approximately 1 to 3% of dynamic pressure. Also, the acoustic wave is cut–off and decays exponentially with axial distance and thus will be of negligible value at the leading edge of the rotor cascade. Thus, these vortical and entropic waves are used to set the linearized unsteady analysis. Harmonic incidence angles on the rotor help show the overall level of unsteadiness due to this distorted flow; incidence variations are roughly ± 2°. The velocity perturbation is 3.0% of the steady relative velocity; we assume that the disturbances are modeled within the linear framework of the analysis.

The Campbell diagram, as obtained from the root strain gages on the two transducer–instrumented blades, is shown in Figures 5a and 5b. The measurements shown were taken at the low operating line (LOL). The test sequence is as follows. The compressor was slowly accelerated to 8800 RPM at the LOL then decelerated to 8100 RPM, the throttle set to the NOL, pressure transducer and strain gage data acquired, and then a slow acceler–

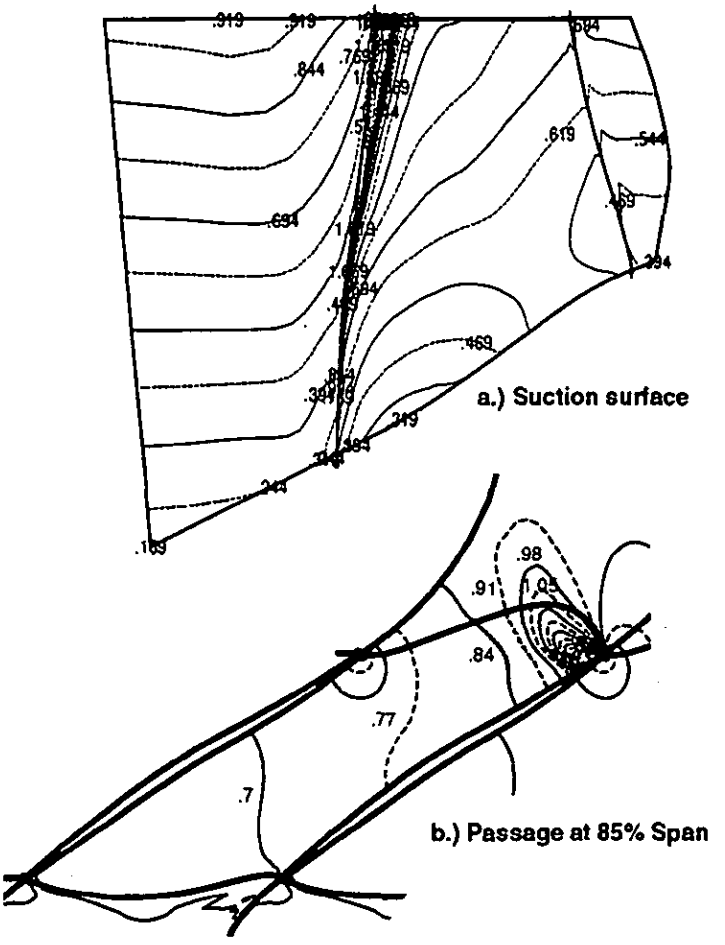

Figure 6. 3D Navier–Stokes predicted contours of Ideal Mach Number

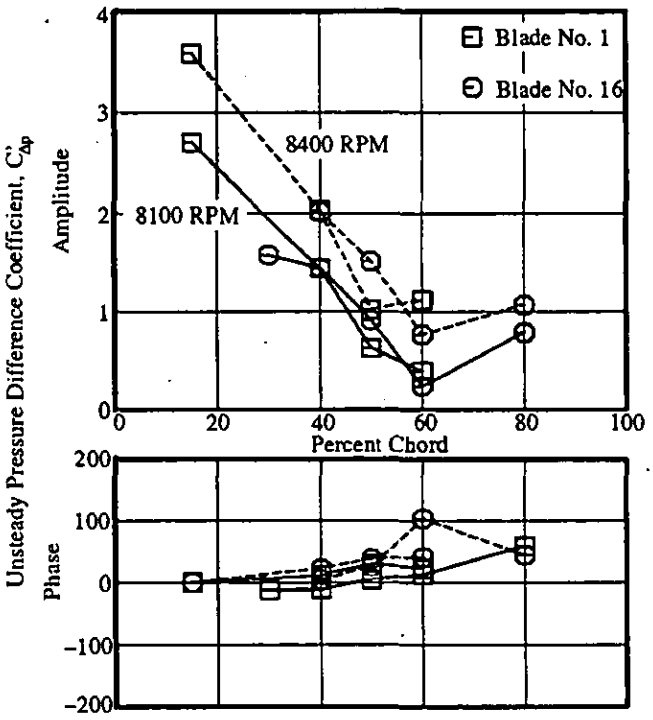

Figure 7. Measured unsteady loading due to 3/rev excitation near 62% speed

tinn to 8400 RPM, followed by another set of transient data being acquired. The speed was then dropped to 8100 RPM, the throttle set back to the LOL setting and the machine shut down. Since, the resonance occurs at approximately 8700 RPM, a full sweep through the resonance was not obtained at the NOL. Therefore to obtain peak resonance frequencies and damping from the strain gage measurements, the LOL data were used and it is assumed that frequencies and total system damping is relatively unchanged between LOL and NOL. For both instrumented blades the difference between LOL and NOL vibrations was less than 5% at 8100 and 8400 RPM and thus, the above is assumed to be valid.

Fnr blade no. 1, close examination of Figure 5a sbows the 1F resonance peak occurred at 8690 RPM (434.5 Hz) and damping (ζ) was calculated to be 0.008, while for blade no. 16, Figure 5b shows the peak was at 8700 RPM (435.0 Hz) and damping was 0.010. The natural frequencies of blades 1 and 16 are nearly identical, 0.1% difference, while the damping differs by 20% to 25%.

At 8100 RPM for the NOL, the peak–to–peak stress determined from the root strain–gages was 5.2 KSI for blade no. 1 and 4.6 KSI for blade no. 16 (a 12% variation). The phase difference between measurements was 71.7°, which is 4.2° greater than what is determined from a three nodal diameter disturbance with 16 blades in the cascade. Calculations using the single–degree–of–freedom (SDOF) motion equation and the damping and peak resonances shown above, give that blade no. 1 should be 2% larger than blade 16 and that the phase difference from the interblade phase angle definition sbould be 0.8°. At 8400 RPM for NOL, the measured stress was 12.2 KSI for blade no. 1 and 9.4 KSI for blade no. 16 (a 26.0% variation). The difference in phase from what the interblade phase angle gives is still 4.2°. The SDOF calculations show the amplitude variations should be 4.0% and the phase difference from the interblade phase angle definition should be 2.3°. Thus slight blade mistuning variations in the damping and peak resonance account for some of the variability of the strain gage measurements.

The first–flex (1F) deflections predicted by the finite element model are shown in Figure 1. The motion is mostly bending with a slight amount of twist. The strain gage was located in a region predicted to have a large unsteady stress gradient. Thus, accurate determination of deflections at other locatinns on the blade may be difficult.

The steady aerodynamics were predicted using the 3D Navier–Stokes solver. Figure 6 sbows the contours of ideal Mach number along the suction surface and the passage at a span roughly corresponding to the location of the chordwise array of pressure transducers, 85% span. A supersonic flow regime is seen just aft of the leading edge. The extent of the leading edge supersonic "bubble" decreases as span is decreased, going from approximately 10% chord at the tip to being nearly gone at 30% span. The flow is predominantly two–dimensional; radially outward flow exists in the suction surface boundary layer just downstream of the shock and over the aft half from centrifuging of the boundary layer fluid.

The measurements of unsteady loading were acquired at two speeds during the approach to resonance, 8100 and 8400. The reduced frequency, k, is 0.90 for both speeds. At 8100RPM, the blade response was roughly

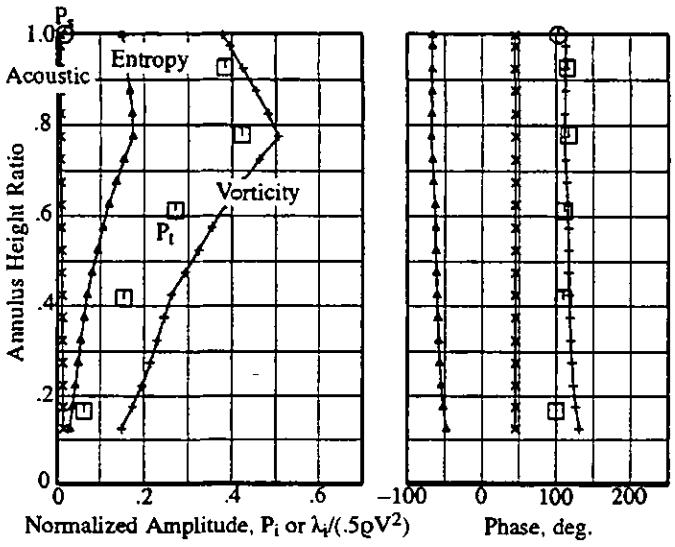

Figure 8. First harmonic of pressures and flow defect characteristics from 8/rev distorted flow at 68% speed

30% of scope limits (allowable values) while at 8400RPM, the response was 60% of scope limits. Figure 7 shows the measured unsteady loading for both 8100 and 8400 RPM. The blade-to-blade variations are negligible with nearly identical chordwise trends occurring for both speeds. The amplitudes of the higher speed, closer to resonance, are approximately one-third higher than those of the lower speed due to the increase in unsteady pressures from the higher amplitude blade vibrations. Predictions from the linearized Euler analysis were not obtainable for this condition.

8/Rev-2F/1T crossing at 68% speed

The spanwise profiles of the first harmonics of the circumferential distributions of total and casing-static pressures, Figure 8, show that the flow disturbance is radially nonuniform in amplitude with a peak value at 77.5% span. The phase is uniform across the span. The acoustic characteristic for this higher frequency distortion is nearly nonexistent, having a value of less than 1% of the dynamic pressure. The vortical and entropic characteristics have similar spanwise trends which correspond to the total pressure profiles. The vortical wave is generally two to three times that of the entropic wave. The rotor incidence angle fluctuations vary across the span from $\pm 1.5°$ at the hub to nearly $\pm 4°$ at 82.5% span. The unsteady velocity perturbation is 7.0% of the steady relative velocity at 85% span.

The measured Campbell diagrams are shown in Figures 9a and 9b for both transducer-instrumented blades at the NOL. Unlike the previous case, slow speed excursions were taken across the nearly full resonance response of the blades, going from 9100 to 10,400 RPM. The speed traverses were slow enough, 15 RPM/sec, to allow for transducer and strain gage data to be acquired and analyzed during any part of the speed range. Therefore, transient data were analyzed at very near the resonance, 9388 RPM, and at a speed that the blade motion was negligible, 9950 RPM, during a slow acceleration. The resonance shows a two peak response which is possibly due to the 8/rev exciting both the 2F mode and the 1T mode which are very close in frequency. For the linearized Euler analysis, two solutions were obtained, one with the motion assumed to be from the 1T mode only and the other with 2F mode only.

The amplitude of the unsteady stress obtained from the blade no. 1

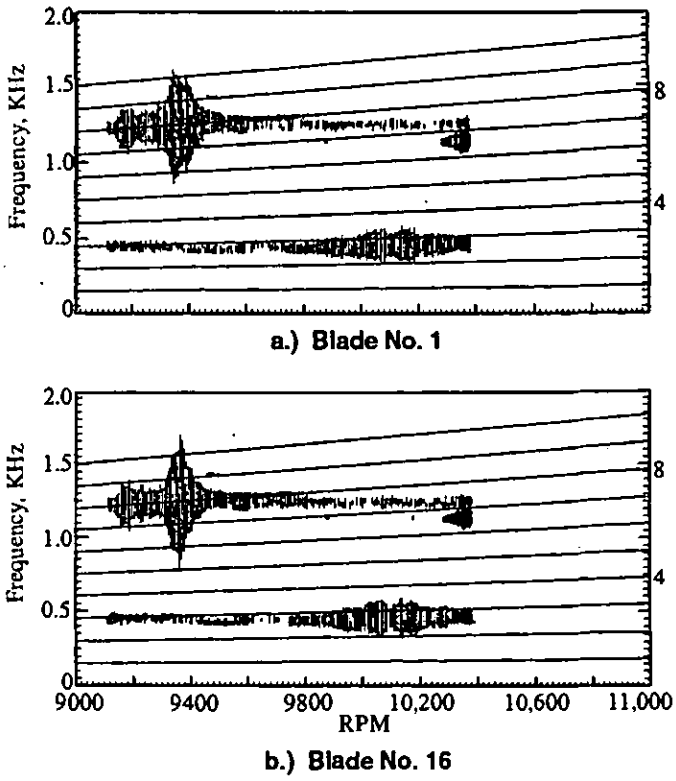

Figure 9. Measured Campbell diagram for 8/rev distortion excitation near 68% speed

gage is 28.4 KSI while for blade no. 16 the measured unsteady stress is 32.2 KSI, showing a 12.7% variability between both blades. The phase difference between the blades is 121.5° which is 58.5° from what is specified by the interblade phase angle, 180°. The peak resonance for blade no. 1 is 9348 RPM (1246 Hz) and the damping (ζ) is 0.0032 while for blade no. 16 the peak occurs at 9261 RPM (1235 Hz) and the damping is 0.0021. Blade no. 1 has a natural frequency of this combined mode that is 1.0% greater than that of blade no. 16 while the damping is 50% greater. The variation in amplitude as calculated from the SDOF equation is 34.0% and the difference in phase from what is prescribed by the interblade phase angle is 1.6°. Theses values differ from what is measured which further shows that the vibrations are a coupled 1T/2F mode since the SDOF equation only applies for single mode vibrations.

Steady flow predictions were obtained at three speeds, one for where the inlet distortion data were acquired, 9100 RPM, and the other two for where the unsteady pressure data were acquired, 9388 RPM and 9950 RPM. At the two lower speeds the predicted flow is very similar to that shown for the 3/rev resonance at 62% speed, showing a supersonic flow "bubble" just aft of the leading edge on the suction side. At 9950 RPM the supersonic "bubble" is gone and is replaced by a nearly normal shock which extends from the leading edge to the suction surface. The steady flow is predominantly 2D along streamline descriptions with only outward radial flow beyond the streamlines being in the suction surface boundary layer.

The steady flow part of the Euler computation was tuned to have its predicted surface Mach numbers nearly match those of the 3D Navier-Stokes analysis. Figures 10a and 10b show the chordwise distribution of

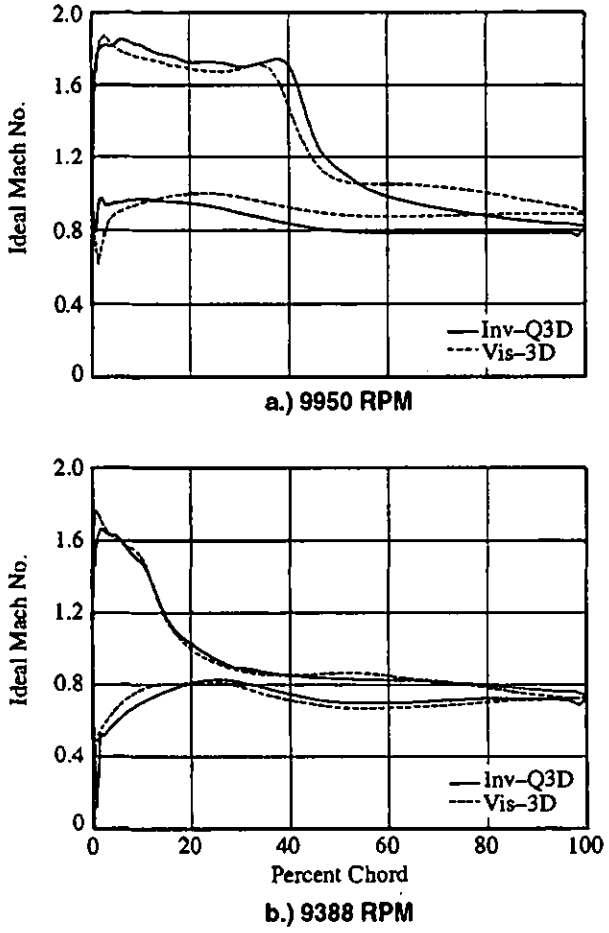

Figure 10. Predicted steady loading on blade near 8/rev crossing at 68% speed

Mach number predicted by the quasi–3d Euler analysis compared to that predicted by the 3D, viscous analysis for both 9950 and 9938 RPM. For 9950 RPM, the tuned quasi–3D Euler matches well with the 3D, viscous solution with both showing the shock centered at approximately 42% chord. At 9388 RPM, the tuned quasi–3D Euler analysis matched well with the viscous solution, with the peak Mach number being 1.6 for the Euler analysis and 1.8 for the viscous analysis. They both showed the shock to be centered at approximately 14% chord.

The predicted and measured unsteady loading response for the off–resonance speed, 9950 RPM (k = 2.28), is shown in Figure 11. The blades have negligible motion and thus, both instrumented blades, no. 1 and 16, have nearly identical unsteady boundary conditions. Good repeatability of measurements is demonstrated by the small differences between blade 1 and 16 measurements. The predictions and measurements show good agreement. The chordwise trends in amplitude and phase are nearly identical. The only differences are the calculations underpredict the increase in amplitude of unsteady loading in front of the shock, around 30% of chord, and over the aft half of the blade the phase predictions are constant while the data increase in value.

For the very near to resonance speed, 9388 RPM (k = 2.38), there is significant blade–to–blade variation between the blade no. 1 and blade no.

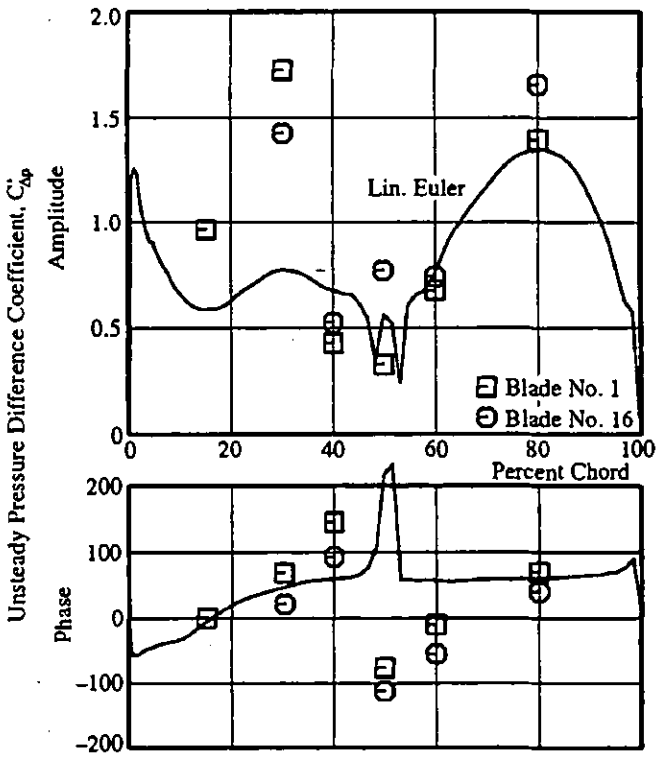

Figure 11. Measured unsteady loading due to 8/rev excitation at 9950 RPM, off resonance

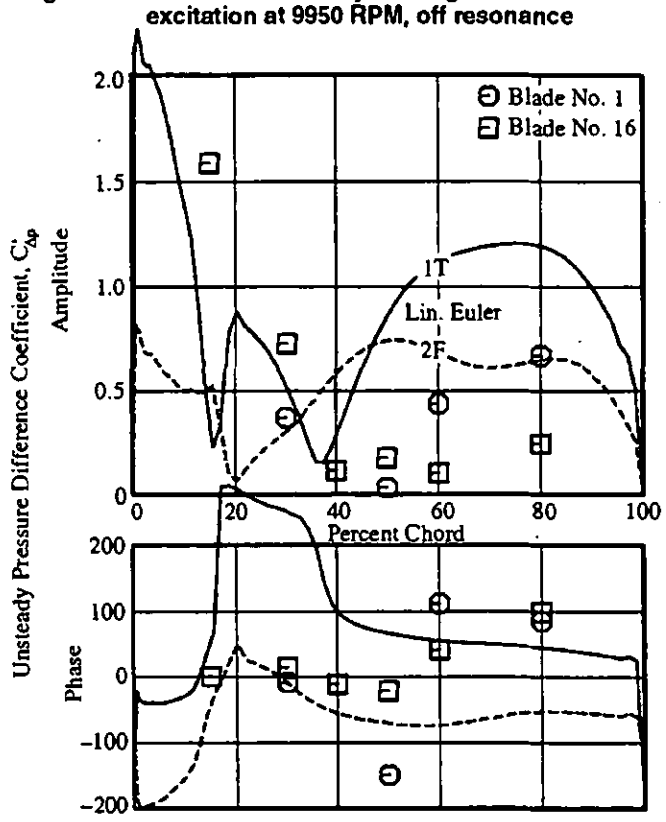

Figure 12. Measured unsteady loading due to 8/rev excitation at 9388 RPM, vear near resonance

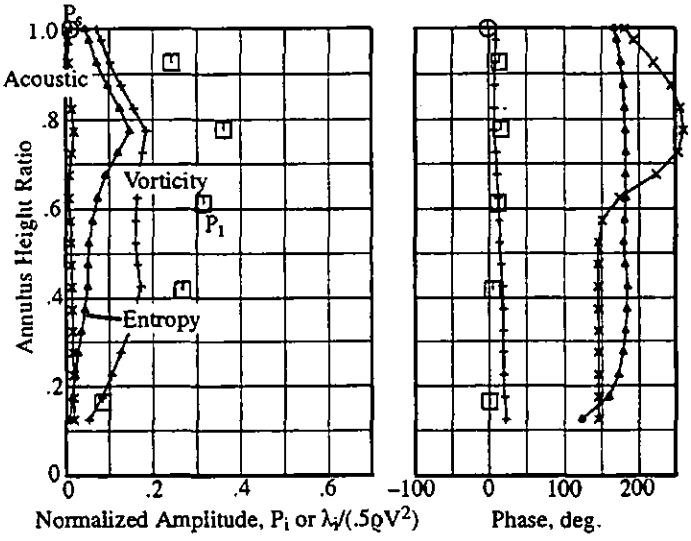

Figure13. First harmonic of pressures and flow defect characteristics from 8/rev distorted flow at 98% speed

16 measurements as can be seen in Figure 12. The strain gage data showed large blade–to–blade variations which would support the variations in unsteady loading measurements between the two blades. The motion of adjacent airfoils was not measured and thus, mistuning effects from blades 2 and 15 cannot be determined.

Predictions of the unsteady loading with both 1T only and 2F only motions were obtained from the linearized–unsteady analysis. The amplitude of the motions used in the analysis were determined from the averages of the blade 1 and blade 16 strain measurements. Significant differences in predicted unsteady loading occur between using 1T and 2F motions with neither solution showing a good comparison with the amplitude and phase data. The true mode is an unknown linear combination of these two modes and thus, the unsteady loading solutions would also be unknown linear combination of the two solutions shown in Figure 12. For this linearized unsteady analysis, blade–to–blade variation in the cascade motions are not modeled and thus, predictions could not compare with both the blade 1 and blade 16 data. Also, 3D unsteady flows can be generated from the blade motion due to the modeshapes, Figure 1, having gradients in the radial direction. These effects are not accounted for in the 2D modeling of the linearized–unsteady analysis.

8/Rev–2S crossing at 98% speed

The spanwise profile of the first harmonic amplitude of the total pressure due to the 8/rev screen at 98 speed is shown in Figure 13. By comparing to the 8/rev distortion data seen at lower speeds, Figure 8, the effect of speed on the distortion is found to be minimal, with nearly identical profiles and a reduction of amplitude of approximately 10%. The speed does affect the characteristics of the disturbance as can be seen by comparing the spanwise profiles of entropy, vorticity and acoustics for the high speed with those at the lower speed. The vorticity wave is decreased in magnitude and is comparable in strength to the entropy wave. The acoustic wave has grown but is still very small. The rotor incidence fluctuations are similar to those of the lower speed. The unsteady velocity harmonic is 3.2% of the steady relative velocity.

The root strain gages were used to measure the unsteady stresses and deflection due to this 2S mode since the trailing edge gages intended for

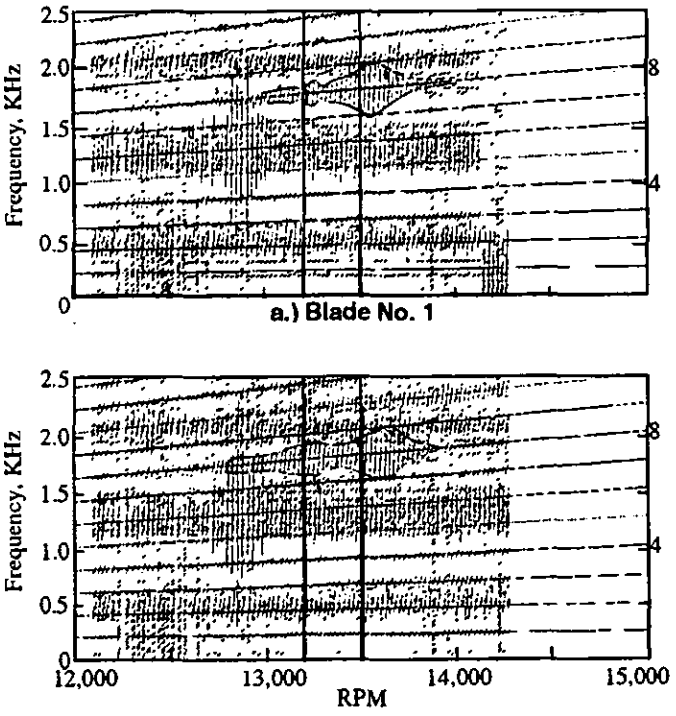

Figure 14. Measured Campbell diagram for 8/rev distortion excitation near 98% speed

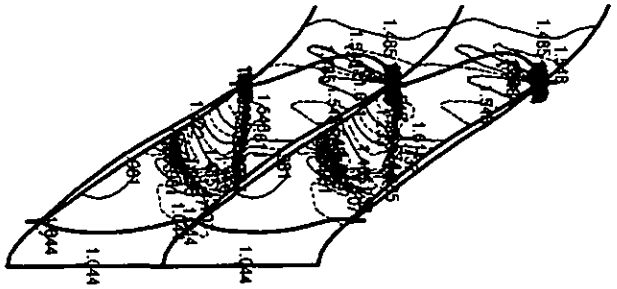

Figure 15. Contours of Ideal Mach number at 85% span for 98% speed

measurement of the chordwise bending modes had failed early in the test. From the finite element model discussed below, the unsteady stress at the gage location is 12% of the highest unsteady stress on the blade which implies that the gages will be marginally acceptable for accurate measurements of strains. The measured Campbell diagrams are shown in Figure 14 for the LOL. Similar to the 62% speed case, the measurements at NOL did not traverse the full extent of the resonance and therefore LOL data will be used to determine peak resonance and damping values. Blade no. 16 shows a double peak response while blade no. 1 shows only a slight "bump" in the response. The peak resonances were 13,550 RPM (1807 Hz) for blade no. 1 and 13,625 (1817 Hz) for blade no. 16 while the damping was 0.0061 for blade no. 1 and 0.0070 for blade no. 16. The natural frequency of blade no. 1 is 0.5% lower than that of blade no. 16 and the damping is 13.0% lower. Phase data for the strain gage measurements were not available for this crossing.

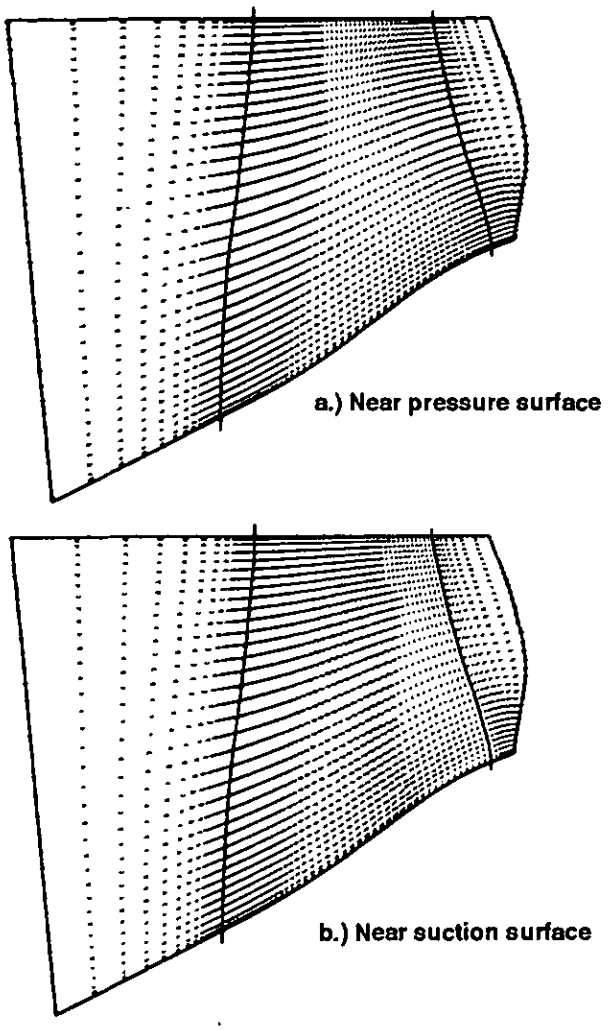

Figure 16. Predicted velocity vectors near blade surfaces

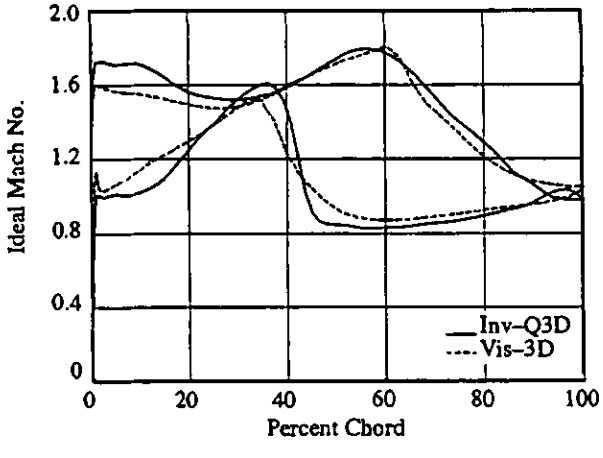

Figure 17. Predicted steady loading on blade near 8/rev crossing at 98% speed

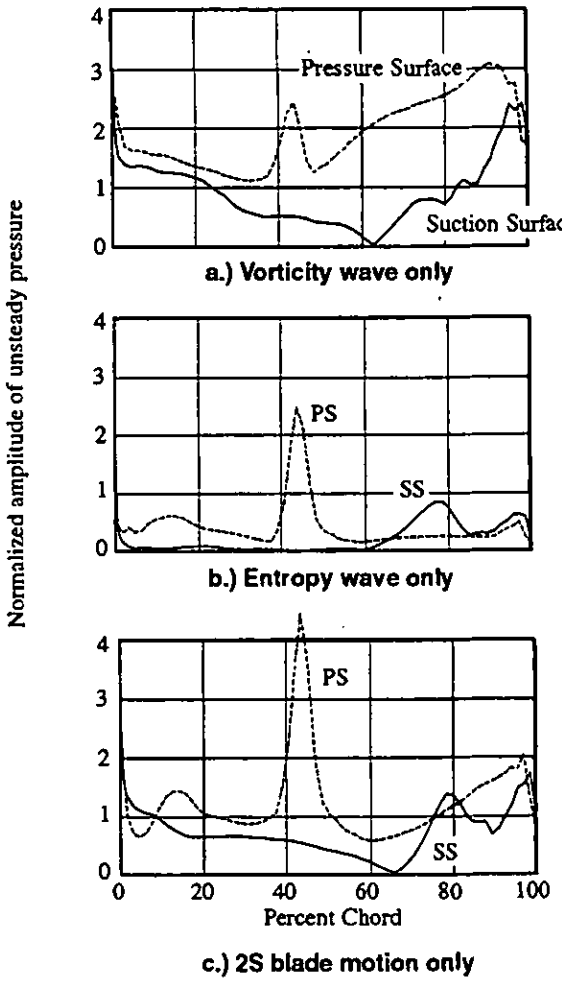

Figure 18. Predicted unsteady pressures on each surface due to each type of unsteadiness

At NOL the transient data were acquired at 13,200 and 13,500 RPM. The reduced frequency for both speeds is 2.30. At the lower speed, the strain gages measured 1.5 KSI unsteady stress for blade no. 1 and 1.4 KSI for blade no.16. At the higher speed, the measured unsteady stress was 3.0 KSI for blade no. 1 and 2.8 KSI for blade no. 16.

The steady flow is strongly supersonic for this high speed, with inlet Mach number of nearly 1.6 and a two shock system in the passage of the blade as seen by the ideal Mach number contours plotted in Figure 15. An oblique shock extends from the leading edge to the suction surface at approximately 75% chord. An in–passage shock is located on the pressure surface at approximately 40% chord. The flow is two–dimensional everywhere except very near the surfaces of the fan. The predicted velocity vectors very near the blade surfaces, shown in Figure 16, demonstrate that the fluid is moving radially outward downstream of the shocks. These radial flows are confined to the boundary layers, within approximately 3.5% of the passage for the pressure surface and approximately 5% of the passage near the suction surface. The steady flow predicted by the Euler solutions was tuned to match the 3D, viscous solutions. The surface Mach number distribution for the quasi–3D Euler analysis is shown compared to the above analysis in Figure 17.

For the 13,200 RPM speed, the amplitudes of the unsteady pressure

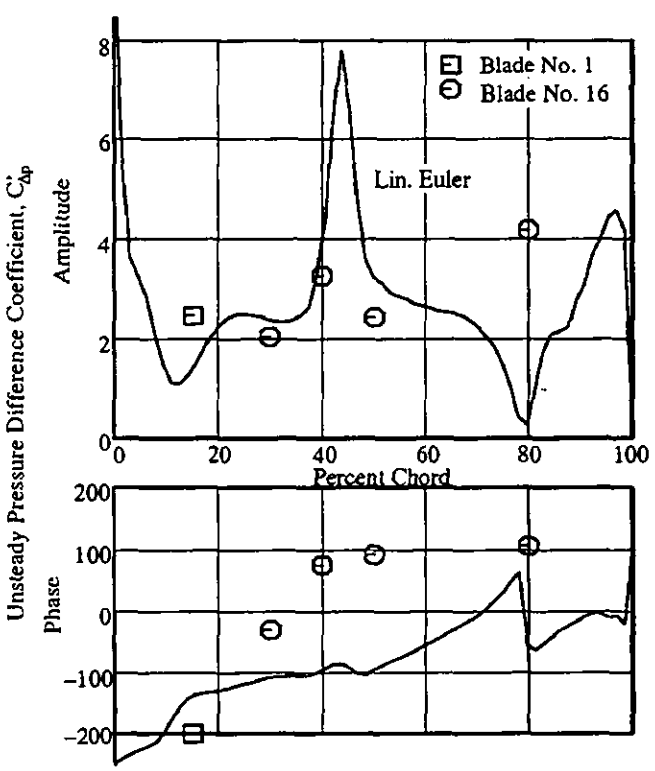

Figure 19. Measured unsteady loading due to 8/rev excitation at 13,200 RPM

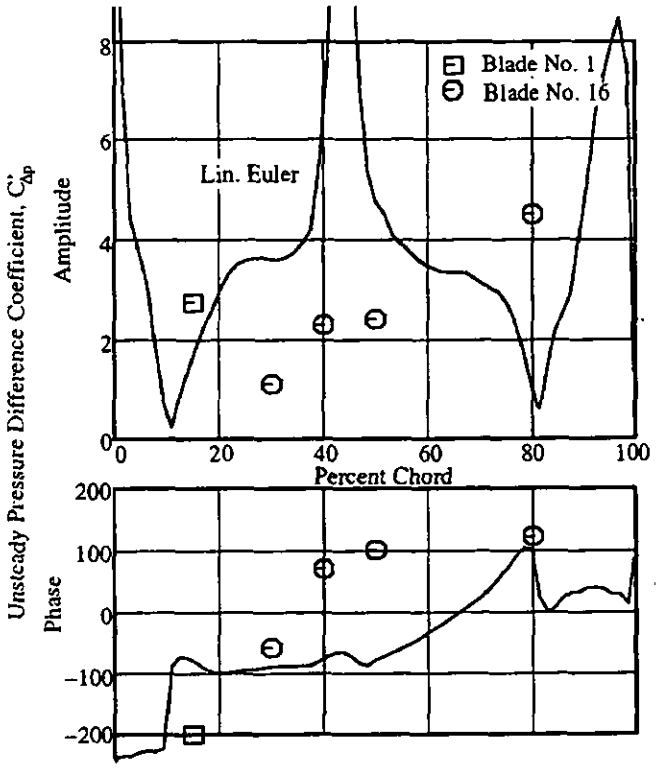

Figure 20. Measured unsteady loading due to 8/rev excitation at 13,500 RPM

chordwise distributions on the pressure and suction surfaces for an entropic wave, a vortical wave and the proper blade motion are presented in Figure 18 to show the relative importance of each to the total unsteadiness acting on the blade surfaces. The unsteady pressures due to the entropy wave are small everywhere except at the pressure surface shock location where the peak in the amplitude is comparable to that generated by the vorticity. The vorticity generates most of the unsteadiness at the trailing edge while at the leading edge both vortical and blade motion give equal levels of unsteady pressure.

Figure 19 shows these solutions combined and the unsteady pressure difference calculated and then compared to the measurements obtained from the differential pressure transducers. The predictions show relatively good comparison with the data. The increase in amplitude at the shock location is predicted; due to the sparsity of data points, the strength at the peak cannot be determined precisely. The increase in amplitude at the aft part of the blade due to the suction surface shock unsteadiness is shown by the data. However, the predictions miss the location of this increase significantly, 10 to 15% of chord. The phase chordwise distributions agree reasonably well, both showing similar increasing phase with chord trends. For current state-of-the-art linearized-unsteady analyses, this is a good comparison, but improvements are still needed. In determining a modal force for calculating the forcing functions, accurate solutions are needed at the blade leading and trailing edges for this 2S mode (deflections are largest at the blade ends). Therefore, inclusion of viscosity in the modeling is needed to accurately determine the unsteady loading in the trailing edge region.

At the higher speed of 13,500 RPM, Figure 20, the comparison between the prediction and the data becomes poorer. The analysis predicts that the unsteady loading due to the pressure surface shock should get larger while the data shows the unsteady loading decreasing at the shock location. Also, the data shows the overall levels of unsteady loading remaining relatively unchanged while the predictions show the unsteady loading increasing. Similar to the previous case, 8/rev at 68% speed, as blade deflections become a more significant part of the calculations, agreement with the data worsens. Unfortunately, phase information about the blade motions was no available and thus, the amount of blade-to-blade variation in phase seen for the lower speed crossing, is not known for this crossing.

SUMMARY AND CONCLUSIONS

A series of experiments were performed on the low-aspect-ratio, transonic, first-stage blade of a two-stage fan. Extensive detailed measurements of the forced response of an airfoil were made for the first time. Namely, the flow defect due to inlet distortions was measured; the resulting blade unsteady loading was obtained from on-blade pressure transducers, and the vibratory response to these unsteady loads was measured with blade mounted strain gages. Measurements were taken at three resonant crossings, i.e., 3/rev -1F at 62% of design speed, 8/rev -2F/1T at 68% speed, and 8/rev - 2S at 98% speed.

The work presented in this paper is the first part of a series of papers that will describe the whole program. In this portion of the work, the measurements and 2D analysis of the unsteady aerodynamics due to gusts and blade motions are presented.

The flow distortions were analyzed to determine the unsteady flow characteristics. Calculations were performed to obtain the vortical, acoustic and entropic parts of the distorted flow. This is the first time that flow defect measurements have been analyzed to give the entropy wave portion of the excitation.

Both the steady and unsteady flows were analyzed with computational models. The steady flow was predicted with a 3D Navier–Stokes solver while the unsteady flow prediction was obtained from a quasi–3D linearized unsteady Euler solution where the base steady flow is modeled with the quasi–3D, non–linear Euler equations. A novel approach was used for setting the base steady flow solutions. The steady loading was tuned to match that of the 3D, viscous solutions which allowed the base steady flow to simulate three–dimensinnal and viscous effects.

The following is a summary of the important conclusions found from this work.

The distortions were shown to be strongly vortical and moderately entropic. The amplitudes of the downstream–going acoustic waves were nearly non–existent.

The steady flow was predominantly two–dimensional. Outward radial flows were confined to the boundary layers near the blade surfaces. In particular, the flow was centrifuged downstream of shocks and in the aft passage region near the suction surface.

Relatively good agreement was seen between the linearized unsteady Euler solutions and the unsteady pressure difference measurements at the "off" resonance speeds. Thus, the method of simulating viscous effects by tuning the base steady Euler solution to a Navier–Stokes steady solution demonstrated that adequate unsteady solutions can be obtained. At 98% speed, improvements in the solutions are still needed near the trailing edge of the blade. This is particularly important for modes where the trailing edge deflections are the dominant part of the motion, as is the case for this 2S mode.

As resonance was approached, the predicted unsteady loading shnwed poorer agreement with the measurements. In particular, for the crossing at 68% speed, which has a coupled 2F and 1T mode, significant blade–to–blade variations in the phase of the vibrations were measured.

Interrogation of the unsteady solution at the high speed showed that both vortical and entropic waves contribute significantly to the unsteady loading where the entropic contribution is mainly in the region of shocks.

Future work on this program will investigate the three–dimensionality of the unsteady flow. As stated above, the steady flow was predominantly 2D. However, the unsteady flow may be three–dimensional and may be contributing to some of the poor comparisons between the 2D analysis and the data. Three dimensionality due to radial gradients in modeshapes and other 3D effects will be determined from in–passage measurements of 3D velocity vectors and predictions from a 3D, linearized unsteady Euler solver. Once a full understanding of the unsteady loading is achieved, a full forced response prediction of the unsteady stresses will be obtained and compared to the measurements. Also the effects of mistuned cascades on the unsteady aerodynamics will be investigated.

ACKNOWLEDGEMENTS

This program was a cooperative effort involving both GE Aircraft Engines and Wright Laboratory at Wright–Patterson Air Force Base. Many people were helpful in ensuring its success. We would like to thank the Wright Laboratory Compressor Research Facility staff for their many contributions to this effort. In particular, we would like to express our appreciation to Mr. Patrick Russler, Mr. Carl
Williams and Dr. Ron Fost for their contribution to the data acquisition and reduction. At GE, the Aeromechanics Group was essential in the planning, design, test monitoring and data analysis. In particular, Dr. Robert Kielb provided guidance and insight throughout the program. We thank Mr. Dave Woehr for his long hours during testing and his help in the analysis of the strain gage data. Also, thanks to Mr. Josef Panovsky for the structural modeling and analysis of the rotor. The authors also wish to thank GE Aircraft Engines for permission to publish this paper.

REFERENCES

Bolcs. A., and Fransson, T.H., 1986, "Aeroelasticity in Turbomachines: Comparison of Theoretical and Experimental Cascade Results," Air Force Office of Scientific Research, AFOSR–TR–87–0605.

Buffum, D.H., and Fleeter, S., 1990, "Aerodynamics of a Linear Oscillating Cascade," NASA TM–103250.

Capece, V.R., and Fleeter, S., 1987, "Unsteady Aerodynamic Interactions in a Multi–Stage Compressor," ASME Paper No. 87–GT–171.

Fleeter, S., Jay, R.L., and Bennett, W.A., 1978, "Rotor Wake Generated Unsteady Aerodynamic Response of a Cnmpressor Stator," ASME Journal nf Engineering for Power, Vol. 100, pp. 664–675.

Fleeter, S., Bennett, W.A., and Jay, R.L., 1980, "The Time–Variant Aerodynamic Response of a Stator Row Including the Effects of Airfoil Camber," ASME Journal of Engineering for Power, Vol. 102, pp. 334–343.

Gallus, H.E., Lambertz, J., and Wallman, T., 1980, "Blade–Row Interaction in an Axial–Flow Subsonic Compressor Stage," ASME Journal of Engineering for Power, Vol. 102, pp. 169–177.

Giles, M. B., 1988, "Calculation of Unsteady Wake/Rotor Interaction," AIAA Journal of Propulsion, Vol. 4, No. 4, pp. 356–362.

Hall, K. C., and Clark, W. S., 1993, "Linearized Euler Predictinns of Unsteady Aerodynamic Loads in Cascades," AIAA Journal, Vol. 31, No. 3, pp. 540–550.

Hall, K. C., Clark, W. S., and Lorence, C. B., 1994, "A Linearized Euler Analysis of Unsteady Transnnic Flows in Turbomachinery," ASME Journal of Turbomachinery, Vol. 116, No. 3, pp. 477–488.

Hall, K. C., and Crawley, E. F., 1989, "Calculation of Unsteady Flows in Turbomachinery Using the Linearized Euler Equations," AIAA Journal, Vol. 27, No. 6, pp. 777–787.

Hall, K. C., and Lorence, C. B., 1993, "Calculation of Three–Dimensional Unsteady Flows in Turbomachinery Using the Linearized Harmonic Euler Equations," ASME Journal of Turbomachinery, Vol. 115, pp. 800–809.

Henderson, G.H., and Fleeter, S., 1993, "Forcing Function Effects on Unsteady Aerodynamic Gust Response: Part 2–Low Solidity Airfoil Row Response," ASME Journal of Turbomachinery, Vol. 115, pp. 751–761.

Holmes, D. G., and Chuang, H. A., 1993, "2D Linearized Harmonic Euler Flow Analysis for Flutter and Forced Response," in: Unsteady Aerodynamics, Aeroacoustics, and Aeroelasticity of Turbomachines and Propellers, H. M. Atassi, ed., Springer–Verlag, New York.

Huff, D. L., 1987, "Numerical Simulations of Unsteady, Viscous, Transonic Flow Over Isolated and Cascaded Sections by Using a Deforming Grid," AIAA Paper No. 89–2805.

Lindquist, D. R., and Giles, M. B., 1994, "Validity of Linearized Unsteady Euler Equations With Shock Capturing," AIAA Journal, Vol. 32, No. 1, pp.46–53.

Manwaring, S.R., and Fleeter, S., 1990, "Inlet Distortion Generated Periodic Aerodynamic Rotor Response," ASME Journal of Turbomachinery, Vol. 112, pp. 298–307.

Manwaring, S.R., and Fleeter, S., 1993, "Rotor Blade Unsteady Aerodynamic Gust Response to Inlet Guide Vane Wakes," ASME Journal of Turbomachinery, Vol. 115, pp. 197–206.

Manwaring, S.R., and Wisler, D.C., 1993, "Unsteady Aerodynamic Gust Response in Compressors and Turbines," ASME Journal of Turbomachinery, Vol. 115, pp. 724–740.

Rai, M. M., 1989, "Three–Dimensional Navier–Stokes Simulations of Turbine Rotor–Stator Interaction: Part I – Methodology, Part II – Results," AIAA Journal of Propulsion, Vol. 5, No. 3, pp. 307–319.

Rabe, D., Bolcs, A., and Russler, P., 1995, "Influence of Inlet Distortion on Transonic Compressor Blade Loading," Joint Propulsion Conference and Exhibit, San Diego, CA, AIAA Paper 95–2461.

Turner, M.G., and Jennions, I.K., 1992 "An Investigation of Turbulence Mndeling in Transonic Fans Including a Novel Implementation of an Implicit k–ε Turbulence Model," ASME Journal of Turbomachinery, Vol. 115, pp. 249–260.

Verdon, J. M., and Caspar, J. R., 1984, "A Linearized Unsteady Aerodynamic Analysis for Transonic Cascades," Journal of Fluid Mechanics, Vol. 149, pp. 403–429.

Whitehead, D. S., 1990, "A Finite Element Solution of Unsteady Two–Dimensional Flow in Cascades," International Journal of Numerical Methods in Fluids, Vol. 10, pp. 13–34.

Whitfield, D. L., Swafford, T. W., and Mulac, R. A., 1987, "Three–Dimensional Unsteady Euler Solutions for Propfans and Counter–rotating Propfans in Transonic Flow," AIAA Paper 87–1197.

Woehr, D.A., and Manwaring, S.R., 1994, *Augmented Damping of Low Aspect Ratio Fans (ADLARF)*, WL–TR–95–2008.